ARTICLE OPEN

Check for updates

Dislocation-position fluctuations in solid ^{4}He as collective variables in a quantum crystal

Maurice de Koning[1,2]✉ and Wei Cai[3]✉

Quantum behavior at mesoscopic length scales is of significant interest, both from a fundamental-physics standpoint, as well as in the context of technological advances. In this light, the description of collective variables comprising large numbers of atoms, but nevertheless displaying non-classical behavior, is a fundamental problem. Here, we show that an effective-Hamiltonian approach for such variables, as has been applied to describe the quantum behavior of coupled qubit/oscillator systems, can also be very useful in understanding intrinsic behavior of quantum materials. We consider lattice dislocations – naturally occurring mesoscopic line defects in crystals – in the prototypical bosonic quantum crystal, solid ^{4}He. For this purpose, we map fully atomistic quantum simulations onto effective one-dimensional Hamiltonians in which the collective dislocation-position variables are represented as interacting, massive quantum particles. The results provide quantitative understanding of several experimental observations in solid ^{4}He.

npj Quantum Materials (2022)7:119 ; https://doi.org/10.1038/s41535-022-00533-8

INTRODUCTION

The discovery of quantum effects on macroscopic scales a century ago, such as superconductivity in Hg and superfluidity in liquid ^{4}He, are among the most dramatic phenomena observed in the history of physics, leading to an enormous leap in our understanding of the fundamental behavior of condensed matter. Today, the development of quantum technologies still maintains a strong focus on systems in which large groups of atoms collectively display quantum behavior. A recent illustration concerns the observation of entanglement of pairs of engineered micrometer-sized vibrating 'drum' membranes, containing trillions of atoms each[1,2]. In this case, the macroscopic position and momentum coordinates of the membranes, which are collective variables of their individual atomic degrees of freedom, manifest quantum behavior. There are many other examples of such effects in manufactured micro-scale systems[3–12], which, in addition to technological interests, also allow exploring the intersection between the quantum and classical worlds.

Aside from quantum effects in large manufactured objects, there has also been a growing interest in intrinsic mesoscopic objects in condensed matter systems, such as lattice dislocations[13–29] – the line defects that carry plastic deformation in crystalline solids[30,31]. Although these 'strings' have an atomic-scale thickness, their linear dimension may span micrometers, extending into the mesoscale realm. Just as in the case of the vibrating drum-membrane systems mentioned above, the large-scale characteristics of dislocations, such as their position, are collective variables involving large numbers of atoms which may also display non-classical behavior. While several studies[16,17,19,20,25,28,32–34] have considered various quantum aspects of dislocation behavior, much less attention has been given to these collective variables themselves, for instance in terms of an effective Hamiltonian constructed from these coordinates[12]. Indeed, such effective Hamiltonians have proved to be very useful in the context of micro-oscillator systems, for instance in describing the coupling between a qubit and a micromechanical oscillator[3,12]. Here, we explore a similar collective-variable approach, but now in the context of naturally occurring mesoscale crystalline defects displaying quantum behavior. The findings corroborate that such an approach can unlock insight that is very difficult to obtain otherwise, representing a promising methodology for understanding quantum behavior of mesoscale objects in general.

As an illustration of this approach we consider the plastic deformation behavior of hexagonal close-packed (hcp) ^{4}He – the prototypical example of a quantum crystal, for which quantum fluctuations dominate over thermal agitation[21,23,24]. We consider the characteristics of basal-plane dislocations, which are known to be responsible for the dominant basal-slip mode of hcp ^{4}He[26,35]. Specifically, we develop an effective quantum description for the position of a perfect basal-plane edge dislocation, which has both the Burgers vector as well as the dislocation line direction contained in the basal plane. In structural terms, these particular dislocation species can lower their elastic energy by dissociating into two Shockley partial dislocations[30,31], i.e., with Burgers vectors smaller than a primitive lattice vector, separated by a ribbon of stacking fault (SF) with a width determined by the shear modulus and the SF energy. While not all dislocation types display such dissociation into partials, we focus on this particular type of dislocation because of its role in the basal slip deformation mode in hcp ^{4}He[26,35].

Because of its dissociated character, the dislocation location is actually described in terms of two position variables, one for each of the two partials. To develop the effective description of this system, we extract the collective position variables of both partials by analyzing the atomic coordinates from fully atomistic path-integral Monte Carlo (PIMC) simulations (Methods), and map the results onto effective one-dimensional Hamiltonians describing the interaction between massive quantum particles. Not only is such a mapping from a quantum description based on individual

[1]Instituto de Física Gleb Wataghin, Universidade Estadual de Campinas, UNICAMP, 13083-859 Campinas, São Paulo, Brazil. [2]Center for Computing in Engineering & Sciences, Universidade Estadual de Campinas, UNICAMP, 13083-861 Campinas, São Paulo, Brazil. [3]Department of Mechanical Engineering, Stanford University, Stanford, CA 94305-4040, USA. ✉email: dekoning@unicamp.br; caiwei@stanford.edu

atoms to one that focuses on collective 'particles' (i.e., partial dislocation positions) a necessary step in the development of a mesoscale model of quantum plasticity, it also provides key insight into the quantum nature of the individual dislocations themselves by allowing their description in terms wave functions and corresponding energy eigenvalues. Carrying out this protocol for both pure ^{4}He as well as in the presence of ^{3}He isotopic impurities, we obtain quantitative insight that is very difficult to extract directly from a fully atomistic description. First, we find that the effective mass of the dislocation-position collective 'particles' is much smaller than classical estimates, rendering the quantum dislocation core to be highly mobile, which is consistent with the experimental observations of giant plasticity[23,26,36,37]. This finding suggests a composite dislocation structure consisting of a light quantum core surrounded by a heavier classical strain field. Furthermore, the low mass results in a high zero-point energy of the vibrational mode for the separation between the two partials, effectively freezing it into the ground state at the temperatures studied here. Finally, also consistent with experimental findings[26,38,39], the presence of ^{3}He impurities induces a dislocation pinning effect that can be closely described in terms of a confining potential. However, instead of current insight, our results indicate that a single impurity is insufficient to hamper dislocation motion, requiring agglomerates containing several ^{3}He impurities.

RESULTS AND DISCUSSION

Atomistic results for pure hcp ^{4}He

All atomistic results are based on a 6048-atom computational cell at a molar volume of 21 cm^3, well into the stability region of the hcp phase at a pressure of ~ 30 bar[23]. The computational cell contains a single perfect basal-plane edge dislocation with Burgers vector $\mathbf{b} = \frac{1}{3}[1\bar{2}10]$, dissociated into two Shockley partial dislocations[30,31] with Burgers vector $\mathbf{b}_p = \frac{1}{3}\langle 1\bar{1}00\rangle$ separated by a SF. Figure 1 a) shows a typical snapshot of the atomic centroid positions (see below) of the dislocation configuration during a PIMC simulation. These basal-plane dislocations are responsible for plastic deformation in the hcp phase of ^{4}He[26,35]. The atoms on the top and bottom surfaces are fixed at perfect crystal positions, preserving the translational symmetry in the direction of dislocation motion and eliminating any spurious image forces on the perfect dislocation[40]. Furthermore, since previous studies[28,41], including calculations based on the worm algorithm for permutation sampling[41], have shown that the role of quantum exchanges for this dislocation type is small, permutation sampling is disabled in the PIMC calculations.

We first consider pure ^{4}He. To determine the partial positions from the atomistic simulations we analyze the atomic displacement profile across the slip plane (Supplementary Note 1), with the resulting x-position being a collective variable of the atomic positions of the two planes adjacent to the glide plane. Figure 2 a) shows the atomistic PIMC evolution of the collective x-coordinates at $T = 0.267$ K determined from the atomic path centroids, which are the 'centers of mass' of the closed paths, as depicted in Fig. 1 b). The centroids are the most classical-like position variables in the path-integral formulation[42,43], filtering out most of the quantum uncertainty. The pair of partials is extremely mobile, even in absence of external stresses, essentially behaving as free particles moving along the x-axis. Even so, due to the elastic interactions (Supplementary Note 7), the motion of both partials is strongly correlated, with the SF width[30,31] showing fluctuations of only ~1 b around the mean value L_0, as shown in Fig. 2 b). We will return to this issue momentarily. To fully characterize these collective variables we need to go beyond their centroids and quantify their intrinsic quantum fluctuations. In the path-integral formalism these are related to the spatial extent of the closed paths[44]. Therefore, the quantum fluctuations in the dislocation position variables are given by the variation among the M path replicas. In principle, these could be determined by using the same displacement analysis employed for the centroids in Fig. 2 a) to the individual time slices. In practice, however, due to the large zero-point fluctuations, it is unfeasible to even discern the crystal structure for individual times slices, let alone recognize dislocations (Supplementary Note 2). Therefore, we first apply Fourier smoothing (Supplementarry Note 2) to the raw atomic paths before using the displacement-analysis. It is important to note that, even though path-smoothing underestimates the true magnitude of the QM fluctuations, it does not restrict the mapping between the atomistic and effective models as long as the same smoothing protocol is applied to both descriptions. The corresponding atomistic histogram for the distribution of the

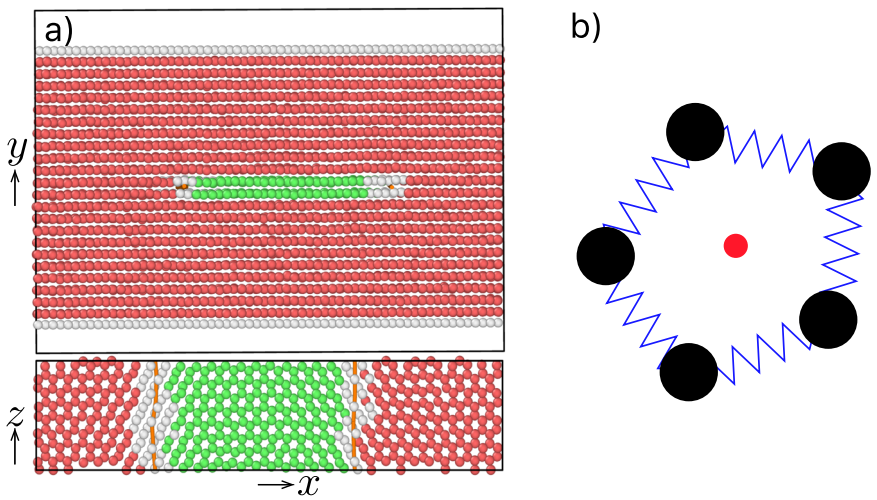

Fig. 1 Simulation cell geometry and centroid definition. a Side and top view of simulation cell, with y-axis along the c-axis and x-axis along the $[1\bar{2}10]$ direction. Cell dimensions in the x, y and z directions are 117.4, 86.2 (including 17.4 Å of vacuum) and 25.4 Å, respectively. Colors of atoms are assigned according to the Common Neighbor Analysis approach[56]. Atoms depicted in red are in hcp surroundings, whereas atoms displayed in green are in an fcc environment and comprise the SF area separating the partials. White atoms indicate atoms in defective regions, either near partial dislocation cores or at free surfaces. Orange lines indicate partial cores. **b** Schematic representation of a closed atomic path in PIMC calculations, with black circles corresponding to system replicas for an example with $M = 5$. Central red circle depicts path 'center of mass' or centroid.

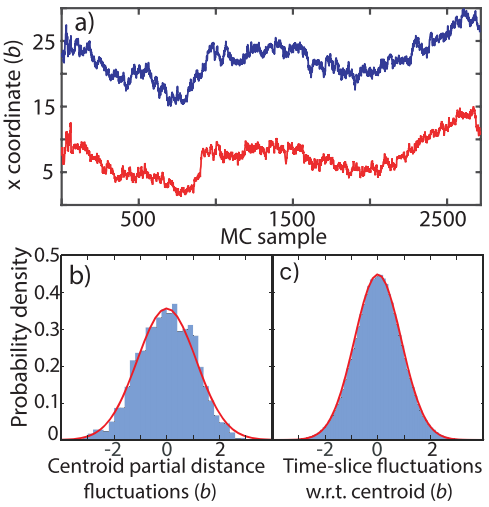

Fig. 2 Partial-dislocation centroid positions and fluctuations and time-slice fluctuations without impurities. a Centroid x-positions of both partials along PIMC run in pure ^{4}He system at $T = 0.267$ K, in units of the perfect Burgers vector $b = 3.667$ Å. **b** Histogram of fluctuations in partial separation obtained from centroids in **a**). **c** Histogram of atomistic time-slice-deviations with respect to centroid for partials using Fourier-smoothed paths (see Supplementary Note 2). Red lines in **b**) and **c**) represent results for effective 1D model in Eq. (1).

Fourier-smoothed time-slice fluctuations in the dislocation position with respect to its centroid is shown in Fig. 2 c). It is found to be identical for both partials, consistent with the fact that both are of the same type. More importantly, however, the smoothed QM fluctuations are larger than the Burgers vector b, such that the partials are delocalized over distances greater than that of the lattice spacing a, indicating that the lattice resistance to their motion is negligible. This is consistent with Fig. 2 a), prior simulations[28] and experimental observations[26].

Effective Hamiltonian for dislocation position coordinates

Next, we develop a quantitative QM description for the collective dislocation position variables. Similar to the approach used in micro-mechanical oscillators[12], we map the atomistic results onto an effective one-dimensional quantum problem of two interacting massive 'particles' whose positions correspond to the collective variables describing the dislocation locations in the atomistic description.

For pure ^{4}He we employ an effective one-dimensional Hamiltonian of the form

$$H_{\text{pure}} = \frac{p_1^2}{2m} + \frac{p_2^2}{2m} + \frac{1}{2}k_e(x_2 - x_1 - L_0)^2, \quad (1)$$

where the subscripts 1 and 2 refer to the particles associated with the left and right partials, respectively. These particles represent dislocation segments of length 25.4 Å, corresponding to four repeat distances along their line direction. Since both partials are of the same type, their masses m are set to be equal. Furthermore, the interaction between both partials is purely elastic, consisting of contributions from the periodic images along the x-axis, as well as from surface images. It can be shown (Supplementary Note 7) that these can be well approximated by an effective harmonic interaction with spring constant k_e and equilibrium separation L_0, which is determined by the shear modulus, the SF energy and periodic images of the dislocations.

The mass m and the spring constant k_e in this model should be chosen such that the corresponding 1D results match the atomistic data as closely as possible. For this purpose, we carry out PIMC simulations for the Hamiltonian of Eq. (1) (Supplementary Notes 3 and 4), discretizing the paths describing particles 1 and 2 using the same number of beads and imaginary-time step as those used in the atomistic simulations at the same temperature $T = 0.267$ K. Using these paths we compute the centroid distance of the variable $x_2 - x_1$ and the time-slice fluctuations in x_1 and x_2 as a function of both k_e and m. As discussed above, the time-slice deviations in x_1 and x_2 that are compared to the atomistic results are those obtained after applying the same path-smoothing protocol employed in the fully atomistic model. The values that best reproduce the atomistic data are found to be $m = 0.292\ m_0$, with m_0 the mass of a single ^{4}He atom and $k_e = 1.6 \times 10^{-2}$ K Å^{-2}. The corresponding 1D-model statistics is in excellent agreement with the atomistic results, as shown in Fig. 2b) and c). The value $m = 0.292\ m_0$ obtained for dislocation segments with lengths over $6b$ is extremely small, being more than three times lower than that of a single ^{4}He atom. Indeed, it is ~ 5 times smaller than the corresponding classical effective-mass value $m_{\text{cl}} \simeq 1.4\ m_0$ (Supplementary Note 8). This difference suggests that both mass values correspond to different physical processes. As the small magnitude of m in the effective model gives rise to large quantum fluctuations in the core position, m can be interpreted as being the effective mass of the quantum dislocation core. The classical mass m_{cl}, on the other hand, results from the increase in the energy of a dislocation moving at a constant velocity relative to its rest state[30]. In the classical theory, this energy appears in the form of kinetic and elastic strain energy of all atoms in the crystal; hence m_{cl} can be interpreted as the effective mass of the strain field of the dislocation. In this view, these findings suggest a composite dislocation structure in which a quantum core with an extremely low mass m is surrounded by a classical strain field with a larger mass m_{cl}. Concerning the stiffness constant, the optimized value for k_e agrees closely with the value $k_e^{\text{iso}} = 1.4 \times 10^{-2}$ K Å^{-2} predicted by isotropic elasticity theory (Supplementary Note 7), which lends further support to the consistency between the effective 1D model and the atomistic simulations.

A fundamental consequence of the mapping approach is that it allows to describe the dislocation system within the standard quantum picture of wave functions and energy eigenvalues for the collective variables. This is possible because the effective Hamiltonian only involves few degrees of freedom so that explicit diagonalization is possible. Moreover, it is significant since it provides information that cannot be readily extracted from atomistic path-integral simulations.

A first example concerns the energy levels of the interacting system described by Eq. (1). It can be decomposed into a non-interacting system containing a free particle and a harmonic oscillator with spring constant $2k_e$, both with the same mass m (Supplementary Note 3). Whereas the former describes the unhampered motion of the perfect edge dislocation as a whole, the latter accounts for the coupling between both partials. For the optimized values of k_e and m, the separation between the energy levels of this coupling is $\Delta E = \hbar\omega = \sqrt{4\hbar^2 k_e/m} = 1.152$ K, meaning, that at 0.269 K, the coupled partial dislocation system is frozen in its ground-state level at $E_0 = 0.576$ K.

Atomistic results for ^{3}He pinning effect

We now turn to the role of ^{3}He impurities, which represents another example in which the wave function approach provides key insight. Although chemically identical to the ^{4}He isotope, due to its lighter mass and corresponding larger zero-point fluctuations, these impurities are known to act as pinning centers that hamper dislocation motion by binding to their cores[27,30,31,38,39,45–48]. This binding effect, at the root of the concept of the Cottrell atmosphere and the associated phenomena of solute drag and precipitation hardening in dislocation theory[30,31,49,50], is due to volumetric strains in the tensile region

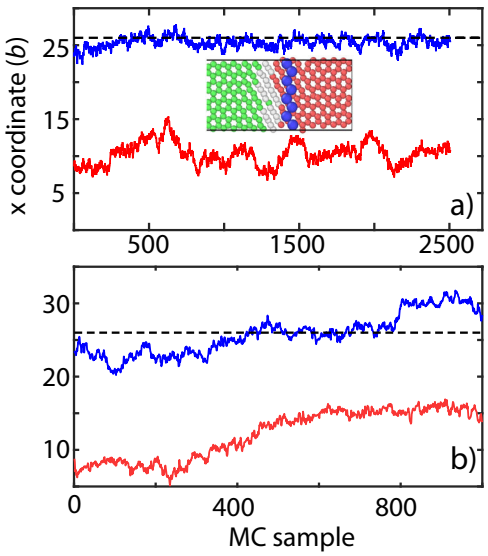

Fig. 3 Partial-dislocation centroids positions with impurities for $T = 0.267$ K and $T = 1.067$ K. a Atomistic centroid dislocation positions in the presence of 2 rows of ^{3}He impurities at $T = 0.267$ K. Horizontal dashed line indicates center position of the two impurity rows. Insets display centroid snapshots of two atomic planes, above and below the glide plane respectively. Meaning of red, green and white colors is the same as in Fig. 1. Blue spheres depict centroids of ^{3}He impurities. **b**) Same as in **a**), but at $T = 1.067$ K.

around a dislocation core with an edge component, which provide increased room for the ^{3}He impurity in the core as compared to a regular lattice site and gives rise to a reduction of zero-point energy. To study this effect, we substitute a number of ^{4}He atoms by the ^{3}He isotope. Given that the binding energy is expected to be very low, with experimental estimates in the range 0.3-0.7 K ($\sim 10^{-5}$ eV)[26,38,39], we insert two adjacent rows of four ^{3}He atoms on the tensile side of the dislocation to enhance the magnitude of the pinning effect, as shown in the inset in Fig. 3 a). Indeed, atomistic simulations carried out using only a single row of ^{3}He impurities were found not to hamper the dislocation in any respect, indicating that, in this case, the binding effect is not sufficiently strong to pin the dislocation.

In the presence of the ^{3}He cluster, the right partial is clearly immobilized at $T = 0.267$ K, as shown by its centroid dislocation position, shown by the blue line, obtained from fully atomistic PIMC calculations in Fig. 3 a). It remains localized at the position of the impurity rows, indicated by the horizontal dashed line, unable to move away from them. While the left partial, shown as the red line, is not explicitly pinned, its mobility is also restricted due to its strong coupling to the trapped right partial, effectively pinning the edge dislocation as a whole. However, as shown in Fig. 3 b), when the temperature is raised to $T = 1.067$ K, the dislocation is able to break free and unpin from the rows of ^{3}He impurities, consistent with the low binding energies observed in experiment.

Effective Hamiltonian for ^{3}He pinning effect

To quantify the pinning effect, we adopt the same approach utilized for the pure ^{4}He case, specifying an effective 1D model that seeks to reproduce the atomistic results. In the presence of the pinning centers, the effective Hamiltonian is augmented by a confining potential $V_{\rm pin}(x_2)$, such that $H = H_{\rm pure} + V_{\rm pin}(x_2)$, where $H_{\rm pure}$ is the optimized Hamiltonian for the pure case. We choose $V_{\rm pin}$ to be a shifted and truncated harmonic potential with force constant $k_{\rm i}$ and energy shift U_0 positioned at the impurity-row center x_0, i.e., $V_{\rm pin}(x) = \min\left[\frac{1}{2}k_{\rm i}(x - x_0)^2 - U_0, 0\right]$, as shown schematically by the red line in Fig. 4 a). Whereas $k_{\rm i}$ controls the magnitude of the dislocation-position fluctuations when it is trapped, the depth U_0 determines how easy/difficult it is for the partial to break free from the pinning center. By first comparing PIMC simulations for this model (Supplementary Notes 5 and 6) to the atomistic PIMC simulations for $T = 0.267$ K, when the dislocation is effectively pinned, we find that $k_{\rm i} = 4.25 \times 10^{-2}$ K Å^{-2} provides a good description of the pinning strength, with both the dislocation-centroid as well as the time-slice fluctuations closely reproducing the atomistic data for both the left and right partials, as shown in Fig. 4 b)-e).

For given values of $k_{\rm e}$, m and $k_{\rm i}$, the value of U_0 now determines whether or not the effective 1D system has at least one localized energy level that corresponds to a trapped dislocation state. To match its value to the atomistic results, the well should be sufficiently deep for the dislocation to be strongly pinned at $T = 0.267$ K, but shallow enough for it to be able to readily escape for $T = 1.067$ K, as depicted in Fig. 3 a) and b). While it is difficult to obtain a precise value for U_0, mostly due to the limited availability of atomistic data to estimate escape probabilities, we find $U_0 = 1.25$ K to give consistent results when considering PIMC runs of 8×10^4 independent samples for the effective 1D system at both temperatures. This is shown in Fig. 4 f), which displays the evolution of the path centroids for the corresponding effective model at $T = 1.067$ K. Similar to the atomistic results of Fig. 3b), the right partial experiences a pinning effect, but it is able to escape during the considered simulation interval, alternating between trapped and untrapped states. Of course, due to the finite width of the trapping potential, the right-partial position still fluctuates when it is trapped.

Having defined the values for the four model parameters it is again useful to resort to the standard quantum description based on wave functions and energy levels of the collective variables. We determine the energy eigenstates $\Psi_{\rm n}(x_1, x_2)$ and eigenvalues $E_{\rm n}$ by numerically solving the stationary Schrödinger eigenvalue problem using a finite-difference method (Supplementary Note 9). Both the ground state and the first excited states at the energy levels $E_0 = -0.143$ K and $E_1 = 0.411$ K are localized at the pinning well. As shown in Fig. 4 a) for the ground state, this localization is established by the peaked nature of the probability-density distributions for the x_2 coordinate, $\Phi_{\rm n}(x_2) \equiv \int dx_1 |\Psi_{\rm n}(x_1, x_2)|^2$. The second excited state, however, is entirely delocalized, with $\Phi_2(x_2)$ displaying a free-particle-like probability density profile. Indeed, its energy eigenvalue $E_2 = 0.576$ K essentially matches that of the ground state of the pure ^{4}He system in which the entire dislocation can move freely.

Based on these results we now estimate the binding strength of the impurity rows from the energy spectrum of the effective 1D model. As the second excited state is the lowest energy state in which the probability density is mostly outside the well, we estimate the binding energy as $E_{\rm b} = E_2 - E_0 \simeq 0.72$ K. This result is consistent with available experimental data, in which $E_{\rm b}$ has been estimated to range between 0.3 and 0.7 K. In addition to the consistency for the binding energetics, the present results suggest that the experimentally observed pinning effect may not be due to isolated ^{3}He atoms but rather requires clusters containing multiple impurities.

In summary, we have characterized the quantum behavior of collective variables describing the positions of two straight Shockley partial dislocations in hcp ^{4}He. By matching atomistic PIMC simulations to effective models in which they are modeled as interacting quantum particles in a 1D space, we obtain fundamental insight into properties of the dislocation cores. In particular, in absence of ^{3}He impurities, the unhampered motion of these dislocations, even in absence of external stresses, can be linked to extremely low effective masses which give rise to large intrinsic quantum fluctuations in the position variables. In the presence of ^{3}He impurities, the 1D mapping provides insight into their role in dislocation pinning. In addition to obtaining a binding

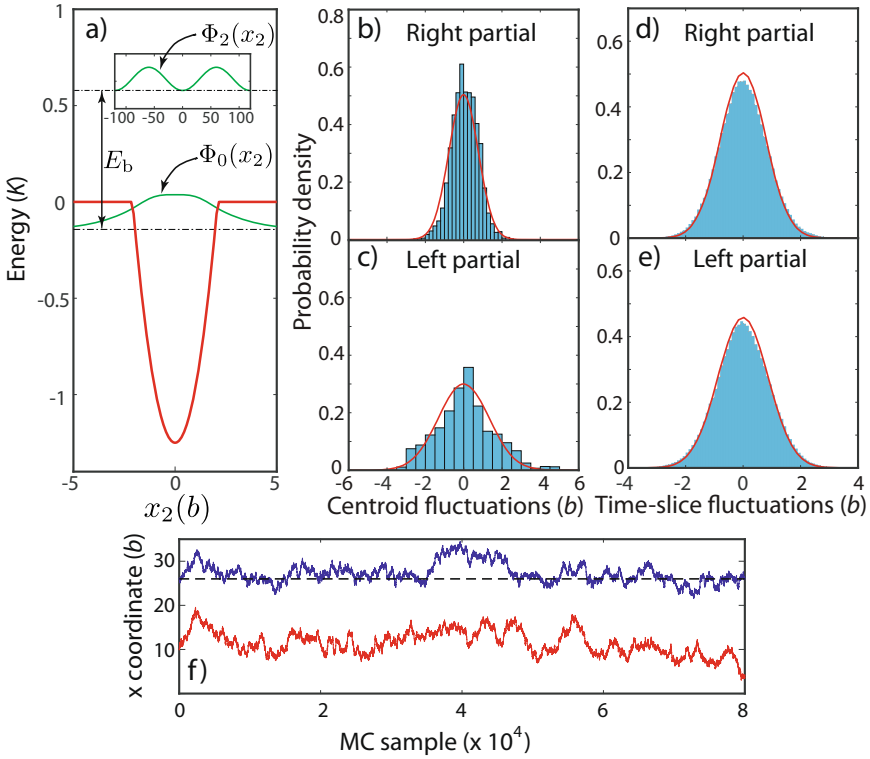

Fig. 4 Eigenstates for effective 1D model with pinning potential and corresponding PIMC results. a Ground-state and second excited-state probability densities for x_2 (green lines) for truncated and shifted harmonic potential (red line) with $k_i = 4.25 \times 10^{-2}$ K Å^{-2} and $U_0 = 1.25$ K. Horizontal dashed lines depict energy levels of states. Histograms in **b** and **c** describe fluctuations in atomistic dislocation centroid positions of the right (pinned) and left partial dislocations, respectively, as obtained from Fourier-smoothed atomistic paths for $T = 0.267$ K. Histograms in **d** and **e** depict statistics of atomistic dislocation time-slice deviations with respect to centroids for right and left partials, respectively, $T = 0.267$ K. Red lines in **b–e** correspond to statistics obtained from 8×10^4 independent paths for the effective 1D model. **f** Centroid positions for variables x_1 (red line) and x_2 (blue line) from PIMC simulation for shifted and truncated pinning potential at $T = 1.067$ K.

energy that is consistent with experimental estimates, the results indicate that the pinning effect may not be due to isolated ^{3}He atoms but rather requires clusters of impurities. Beyond the specific insight into dislocation properties in ^{4}He, which could not have been inferred from an entirely atomistic description, the results highlight the potential of effective models involving collective variables in elucidating the quantum behavior of mesoscale objects, in particular with regard to the possibility of describing them in terms of wave functions and energy eigenvalues. Indeed, in the specific context of understanding the physics of solid He, the effective Hamiltonian approach should also be useful to comprehend the dislocation behavior of the body-centered cubic (bcc) phase of solid ^{3}He. In this case, it is the ^{4}He atoms that act as isotopic impurities and are able to hamper dislocation motion[51]. In addition to the fact that dislocations in bcc lattice behave very differently from those in hcp structures, the fermionic nature of the ^{3}He host crystal as well as the smaller zero-point vibrations of the ^{4}He impurities pose an interesting challenge.

METHODS

Atomistic PIMC simulations

The path-integral Monte Carlo method[52] is a numerical implementation of Feynman's imaginary-time path-integral formulation of quantum statistical mechanics[42,43,53], which transforms the quantum problem into an equivalent classical one in which each atom is described by a closed path along the imaginary-time axis. In the PIMC approach these paths are discretized in terms of M imaginary-time slices, giving rise to 'polymer' chains consisting of M system replicas connected by harmonic springs, as shown schematically in Supplementary Figure 1. The properties of the quantum system are then obtained by statistical sampling of these polymer-chain conformations. In the analysis of the results, the so-called path centroids, visualized in Supplementary Figure 1, are often useful since they filter out much of the quantum uncertainty[44]. All atomistic calculations in this work have been carried out using the implementation provided by the PIMC++ code[54] using a pair action based on the Aziz-potential[55] with a cutoff of 8 Å and a path discretization in terms of $M = 150$ time slices and an imaginary time step $\tau = \beta/M$, with $\beta \equiv 1/k_B T$ the inverse temperature. Path sampling is carried out within the isothermal-isostress ensemble[28] at zero imposed stress, sampling only shear deformations in the basal plane and using the bisection algorithm for path updates[52]. Since bosonic exchange effects have been found to be negligible for these basal-plane dislocation cores in hcp ^{4}He in previous studies[28,41], permutation sampling is disabled.

PIMC Simulations Of Effective 1D model For Pure ^{4}He

For the effective 1D Hamiltonian of the pure ^{4}He system given by

$$H_{\text{pure}} = \frac{p_1^2}{2m} + \frac{p_2^2}{2m} + \frac{1}{2}k_e(x_2 - x_1 - L_0)^2, \tag{2}$$

it is useful to employ the normal-mode coordinate transformation

$$\tilde{x}_1 \equiv \frac{1}{\sqrt{2}}(x_1 + x_2), \tag{3}$$

and

$$\tilde{x}_2 \equiv \frac{1}{\sqrt{2}}(x_2 - x_1). \tag{4}$$

The transformed Hamiltonian then becomes

$$H_{\text{pure}} = \frac{\tilde{p}_1^2}{2m} + \frac{\tilde{p}_2^2}{2m} + \frac{1}{2}(2\,k_e)(\tilde{x}_2 - L_0)^2, \tag{5}$$

decoupling the problem of two interacting particles into one of non-interacting particles, namely a free particle and a harmonic oscillator with a force constant that is twice the value for the interacting problem, both with the mass m. In this way, the interacting particle system is most effectively treated by independently simulating the free particle and harmonic oscillator systems. Since the density matrices for both the free-particle case and the harmonic oscillator are known analytically, the PIMC calculations can be carried out using the Lévy construction, which is a rejection-free path sampling algorithm in which successive path samples are statistically independent. In this way, paths for $\tilde{x}_1$ and $\tilde{x}_2$ are sampled independently, as detailed in the Supplementary Note 3, after which the position variables for the interacting particles are obtained using the inverse normal-mode transformation

$$x_1 = \frac{1}{\sqrt{2}}(\tilde{x}_1 - \tilde{x}_2), \tag{6}$$

and

$$x_2 = \frac{1}{\sqrt{2}}(\tilde{x}_1 + \tilde{x}_2). \tag{7}$$

PIMC Simulations Of Effective 1D model with ^{3}He Impurities

In the presence of ^{3}He impurities the effective 1D Hamiltonian is given by

$$H = \frac{p_1^2}{2m} + \frac{p_2^2}{2m} + \frac{1}{2}k_e(x_2 - x_1 - L_0)^2 + V_{\text{pin}}(x_2), \tag{8}$$

with

$$V_{\text{pin}}(x) = \min\left[\frac{1}{2}k_i(x - x_0)^2 - U_0, 0\right]. \tag{9}$$

In this case, due to the truncated character of V_{pin}, the problem cannot be decoupled into two independent non-interacting problems. Accordingly, a PIMC simulation of this system requires explicit simultaneous treatment of x_1 and x_2. Here we achieve this using a basic Markov chain path-sampling algorithm (Supplementary Note 6).

DATA AVAILABILITY

The data that support the findings of this study are available at https://doi.org/10.5281/zenodo.7390438

CODE AVAILABILITY

All numerical codes used in this paper are available upon request from the authors.

Received: 23 August 2022; Accepted: 9 December 2022;
Published online: 27 December 2022

REFERENCES

1. Kotler, S. et al. Direct observation of deterministic macroscopic entanglement. *Science* **372**, 622–625 (2021).
2. Berkowitz, R. Macroscopic systems can be controllably entangled and limitlessly measured. *Phys. Tod.* **74**, 16–18 (2021).
3. Ashhab, S. & Nori, F. Qubit-oscillator systems in the ultrastrong-coupling regime and their potential for preparing nonclassical states. *Phys. Rev. A* **81**, 042311 (2010).
4. Ball, P. Entangled diamonds vibrate together. Nature (2011). https://doi.org/10.1038/nature.2011.9532.
5. Lee, K. C. et al. Entangling macroscopic diamonds at room temperature. *Science* **334**, 1253–1257 (2011).
6. Teufel, J. D. et al. Sideband cooling of micromechanical motion to the quantum ground state. *Nature* **475**, 359–363 (2011).
7. Hoff, U. B., Kollath-Bönig, J., Neergaard-Nielsen, J. S. & Andersen, U. L. Measurement-induced macroscopic superposition states in cavity opto-mechanics. *Phys. Rev. Lett.* **117**, 143601 (2016).
8. Sarma, B. & Sarma, A. K. Ground-state cooling of micromechanical oscillators in the unresolved-sideband regime induced by a quantum well. *Phys. Rev. A* **93**, 033845 (2016).
9. Ornes, S. News feature: Quantum effects enter the macroworld. *Proc. Natl Acad. Sci. U. S. A.* **116**, 22413–22417 (2019).
10. Yu, H. et al. Quantum correlations between light and the kilogram-mass mirrors of LIGO. *Nature* **583**, 43–47 (2020).
11. Gely, M. & Steele, G. A. A massive squeeze. *Nat. Phys.* **17**, 299–300 (2021).
12. Ma, X., Viennot, J. J., Kotler, S., Teufel, J. D. & Lehnert, K. W. Non-classical energy squeezing of a macroscopic mechanical oscillator. *Nat. Phys.* **17**, 322–326 (2021).
13. Kubamoto, E., Aono, Y., Kitajima, K., Maeda, K. & Takeuchi, S. Thermally activated slip deformation between 0.7 and 77 k in high-purity iron single crystals. *Philos. Mag. A* **39**, 717–724 (1979).
14. Takeuchi, S., Hashimoto, T. & Maeda, K. Plastic deformation of bcc metal single crystals at very low temperatures:. *Trans. Jpn. Inst. Met.* **23**, 60–69 (1982).
15. Caillard, D. On the stress discrepancy at low-temperatures in pure iron. *Acta Mater.* **62**, 267–275 (2014).
16. Proville, L., Rodney, D. & Marinica, M.-C. Quantum effect on thermally activated glide of dislocations. *Nat. Mater.* **11**, 845–849 (2012).
17. Barvinschi, B., Proville, L. & Rodney, D. Quantum peierls stress of straight and kinked dislocations and effect of non-glide stresses. *Modell. Simul. Mater. Sci. Eng.* **22**, 025006 (2014).
18. Landeiro Dos Reis, M., Choudhury, A. & Proville, L. Ubiquity of quantum zero-point fluctuations in dislocation glide. *Phys. Rev. B* **95**, 094103 (2017).
19. Freitas, R., Asta, M. & Bulatov, V. V. Quantum effects on dislocation motion from ring-polymer molecular dynamics. *npj Comput. Mater.* **4**, 55 (2018).
20. Corboz, P., Pollet, L., Prokof'ev, N. V. & Troyer, M. Binding of a ^{3}He impurity to a screw dislocation in solid ^{4}He. *Phys. Rev. Lett.* **101**, 155302 (2008).
21. Cazorla, C. & Boronat, J. Simulation and understanding of atomic and molecular quantum crystals. *Rev. Mod. Phys.* **89**, 035003 (2017).
22. Sempere, S., Serra, A., Boronat, J. & Cazorla, C. Dislocation structure and mobility in hcp rare-gas solids: Quantum versus classical. *Crystals* **8**, 64 (2018).
23. Beamish, J. & Balibar, S. Mechanical behavior of solid helium: Elasticity, plasticity, and defects. *Rev. Mod. Phys.* **92**, 045002 (2020).
24. Balibar, S. Supersolid helium: Stiffer but flowing. *Nat. Phys.* **5**, 534–535 (2009).
25. Pessoa, R., Vitiello, S. A. & de Koning, M. Dislocation mobility in a quantum crystal: The case of solid ^{4}He. *Phys. Rev. Lett.* **104**, 085301 (2010).
26. Haziot, A., Rojas, X., Fefferman, A. D., Beamish, J. R. & Balibar, S. Giant plasticity of a quantum crystal. *Phys. Rev. Lett.* **110**, 035301 (2013).
27. Fefferman, A. D., Souris, F., Haziot, A., Beamish, J. R. & Balibar, S. Dislocation networks in ^{4}He crystals. *Phys. Rev. B* **89**, 014105 (2014).
28. Landinez Borda, E. J., Cai, W. & de Koning, M. Dislocation structure and mobility in hcp ^{4}He. *Phys. Rev. Lett.* **117**, 045301 (2016).
29. Kuklov, A. B., Pollet, L., Prokof'ev, N. V. & Svistunov, B. V. Supertransport by superclimbing dislocations in ^{4}He: When all dimensions matter. *Phys. Rev. Lett.* **128**, 255301 (2022).
30. Hirth, J. P. & Lothe, J.Theory of Dislocations (Krieger Publishing Company, 1992), 2 edn.
31. Hull, D. & Bacon, D.Introduction to dislocations (Butterworth-Heinemann, 2001).
32. Suzuki, T. Quantum theory of dislocation motion in metals. *J. Phys. Soc. Jpn.* **64**, 2817–2827 (1995).
33. Suzuki, T. Quantum theory of dislocation motion in crystals. *J. Phys. Soc. Jpn.* **65**, 2526–2531 (1996).
34. de Gennes, P.-G. Quantum dynamics of a single dislocation. *C. R. Phys.* **7**, 561–566 (2006).
35. Paalanen, M. A., Bishop, D. J. & Dail, H. W. Dislocation motion in hcp ^{4}He. *Phys. Rev. Lett.* **46**, 664–667 (1981).
36. Zhou, C. et al. Comment on "giant plasticity of a quantum crystal". *Phys. Rev. Lett.* **111**, 119601 (2013).
37. Haziot, A., Rojas, X., Fefferman, A. D., Beamish, J. R. & Balibar, S. Reply to comment on "giant plasticity of a quantum crystal". *Phys. Rev. Lett.* **111**, 119602 (2013).
38. Day, J. & Beamish, J. Low-temperature shear modulus changes in solid 4he and connection to supersolidity. *Nature* **450**, 853–856 (2007).

39. Iwasa, I. & Kojima, H. Nonlinear and hysteretic ultrasound propagation in solid ^{4}He: Dynamics of dislocation lines and pinning impurities. *Phys. Rev. B* **102**, 214101 (2020).
40. Cai, W., Bulatov, V. V., Chang, J., Li, J. & Yip, S. Periodic image effects in dislocation modelling. *Philos. Mag.* **83**, 539–567 (2003).
41. Pollet, L. et al. Local stress and superfluid properties of solid ^{4}He. *Phys. Rev. Lett.* **101**, 097202 (2008).
42. Feynman, R.Statistical Mechanics: A Set Of Lectures (Westview Press, 1998).
43. Feynman, R. P., Hibbs, A. R. & Styer, D. F.Quantum Mechanics and Path Integrals (Dover Publications, 2010).
44. Gillan, M. J. The path-integral simulation of quantum systems. In Catlow, R., Parker, S. C. & Allen, M. P. (eds.) *Computer Modelling of Fluids Polymers and Solids*, 155 (Kluwer Academic Publishers, 1989).
45. Syshchenko, O., Day, J. & Beamish, J. Elastic properties of solid helium. *J. Phys.: Condens. Matter* **21**, 164204 (2009).
46. Kang, E. S. H., Kim, D. Y., Kim, H. C. & Kim, E. Stress- and temperature-dependent hysteresis of the shear modulus of solid helium. *Phys. Rev. B* **87**, 094512 (2013).
47. Haziot, A., Fefferman, A. D., Beamish, J. R. & Balibar, S. Dislocation densities and lengths in solid ^{4}He from elasticity measurements. *Phys. Rev. B* **87**, 060509 (2013).
48. Iwasa, I. & Suzuki, H. Sound velocity and attenuation in hcp 4he crystals containing 3he impurities. *J. Phys. Soc. Jpn.* **49**, 1722–1730 (1980).
49. Cottrell, A. H. & Bilby, B. A. Dislocation theory of yielding and strain ageing of iron. *Proc. Phys. Soc. Lond., Sect. A* **62**, 49–62 (1949).
50. Gladman, T. Precipitation hardening in metals. *Mater. Sci. Technol.* **15**, 30–36 (1999).
51. Cheng, Z. G. & Beamish, J. Shear modulus and dislocation effects in bcc ^{3}He. *J. Low. Temp. Phys.* **205**, 263–278 (2021).
52. Ceperley, D. M. Path integrals in the theory of condensed Helium. *Rev. Mod. Phys.* **67**, 279–335 (1995).
53. Krauth, W. *Statistical Mechanics: Algorithms and Computations*. (Oxford University Press, Oxford, 2006).
54. Clark, B. K. & Ceperley, D. M. Path integral calculations of vacancies in solid helium. *Comput. Phys. Commun.* **179**, 82–88 (2008).
55. Aziz, R. A., Janzen, A. R. & Moldover, M. R. Ab initio calculations for Helium: a standard for transport property measurements. *Phys. Rev. Lett.* **74**, 1586–1589 (1995).
56. Faken, D. & Jónsson, H. Systematic analysis of local atomic structure combined with 3d computer graphics. *Comput. Mater. Sci.* **2**, 279–286 (1994).

ACKNOWLEDGEMENTS

M.K. acknowledges support from CNPq, Fapesp grant no. 2016/23891-6 and the Center for Computing in Engineering & Sciences - Fapesp/Cepid no. 2013/08293-7. W.C. acknowledges support from the U.S. Department of Energy, Office of Basic Energy Sciences, Division of Materials Sciences and Engineering under Award No. DE-SC0010412.

AUTHOR CONTRIBUTIONS

M.K. and W.C. contributed equally to this work.

COMPETING INTERESTS

The authors declare no competing interests.

ADDITIONAL INFORMATION

Supplementary information The online version contains supplementary material available at https://doi.org/10.1038/s41535-022-00533-8.

Correspondence and requests for materials should be addressed to Maurice de Koning or Wei Cai.

Reprints and permission information is available at http://www.nature.com/reprints

Publisher's note Springer Nature remains neutral with regard to jurisdictional claims in published maps and institutional affiliations.

Open Access This article is licensed under a Creative Commons Attribution 4.0 International License, which permits use, sharing, adaptation, distribution and reproduction in any medium or format, as long as you give appropriate credit to the original author(s) and the source, provide a link to the Creative Commons license, and indicate if changes were made. The images or other third party material in this article are included in the article's Creative Commons license, unless indicated otherwise in a credit line to the material. If material is not included in the article's Creative Commons license and your intended use is not permitted by statutory regulation or exceeds the permitted use, you will need to obtain permission directly from the copyright holder. To view a copy of this license, visit http://creativecommons.org/licenses/by/4.0/.

© The Author(s) 2022